arXiv:1411.4893v2 [cond-mat.dis-nn] 18 Feb 2015

Understanding the ideal glass transition: Lessons from an equilibrium study of hard disks in a channel

M. J. Godfrey and M. A. Moore
School of Physics and Astronomy, University of Manchester, Manchester M13 9PL, UK
(Dated: February 19, 2015)

We use an exact transfer-matrix approach to compute the equilibrium properties of a system of hard disks of diameter σ confined to a two-dimensional channel of width $1.95\,\sigma$ at constant longitudinal applied force. At this channel width, which is sufficient for next-nearest-neighbor disks to interact, the system is known to have a great many jammed states. Our calculations show that the longitudinal force (pressure) extrapolates to infinity at a well-defined packing fraction ϕ_K that is less than the maximum possible $\phi_{\max}$, the latter corresponding to a buckled crystal. In this quasi-one-dimensional problem there is no question of there being any *real* divergence of the pressure at ϕ_K. We give arguments that this avoided phase transition is a structural feature – the remnant in our narrow channel system of the hexatic to crystal transition – but that it has the phenomenology of the (avoided) ideal glass transition. We identify a length scale $\tilde{\xi}_3$ as our equivalent of the penetration length for amorphous order: In the channel system, it reaches a maximum value of around $15\,\sigma$ at ϕ_K, which is larger than the penetration lengths that have been reported for three dimensional systems. It is argued that the α-relaxation time would appear on extrapolation to diverge in a Vogel–Fulcher manner as the packing fraction approaches ϕ_K.

PACS numbers: 05.20.–y, 64.70.Q–, 61.43.Fs

I. INTRODUCTION

There is a long history of studying exactly soluble one-dimensional models in statistical physics. While sometimes these models are interesting in their own right, the main motive for their study is usually to cast some light upon behavior in higher, more physical dimensions d, such as $d = 2$ and $d = 3$, where exact solutions cannot usually be found. In this paper we study a quasi-one-dimensional system of N hard disks of diameter σ confined by impenetrable walls separated by distance $H_d = \sigma + h$, where h is the width of the region containing the centers of the disks (see Fig. 1). For $\sqrt{3}\,\sigma/2 < h < \sigma$, a disk may make contact with its nearest- and next-nearest-neighbor (NNN) disks, but neighboring disks cannot pass each other. The ordering of the disks is still preserved: $0 \le x_1 < x_2 < \ldots < x_N \le L$, where x_i is the position of the center of disk i, measured along the channel, and L is the total length available to the disk centers. The transverse coordinates of the disk centers are denoted by y_i, where $|y_i| \le h/2$. We have in an earlier paper studied the case when $h < \sqrt{3}\,\sigma/2$, which permits only nearest-neighbor (NN) contacts [1]. All our results and figures for the NNN model are for $H_d = 1.95\,\sigma$.

The numbering 1, 2, 3, ..., N of the disks follows the ordering of their x coordinates. In Fig. 2(a), the first disk interacts with its nearest neighbor, the second disk, but it also interacts with another disk, the third disk, giving rise to a NNN coupling. If instead we had $h < \sqrt{3}\,\sigma/2$, such NNN couplings would not be possible: we call this case the *NN model*. Thus, the NN and NNN models describe disks in narrow channels of different widths.

For spin glasses, NNN interactions between the spins in a one-dimensional system can introduce frustration. Suppose we have spins 1, 3, 5, ... in the lower of two rows of spins, and spins 2, 4, 6, ... in the upper row, as shown below:

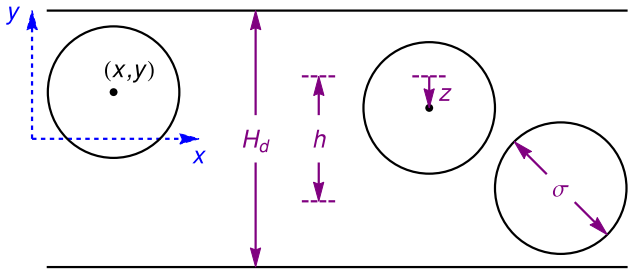

FIG. 1: (Color online) Explanation of the notation used in this paper. Here H_d is the width of the channel, σ is the diameter of each disk, and $h = H_d - \sigma$ is the width of the channel accessible to the centers of the disks. We choose coordinates (x, y) for each disk, where y is measured from the center line of the channel. The distance z is the displacement of the center of a disk from the line of the largest possible displacement of a center from the middle of the channel, i.e., $z = h/2 - y$.

$$\begin{array}{ccccccc} & 2 & & 4 & & 6 & \\ 1 & & 3 & & 5 & & 7 \end{array}$$

With NNN interactions, spin 3 interacts with both of its nearest neighbors 2 and 4, but also with its next-nearest neighbors 1 and 5. This spin system has the same topology of interactions as will be found for some arrangements of the disks in the narrow channel system. While the spin system is effectively one dimensional, the spins in the triangles 1–2–3 and 2–3–4 could be frustrated with appropriate spin couplings. Frustration is regarded as a

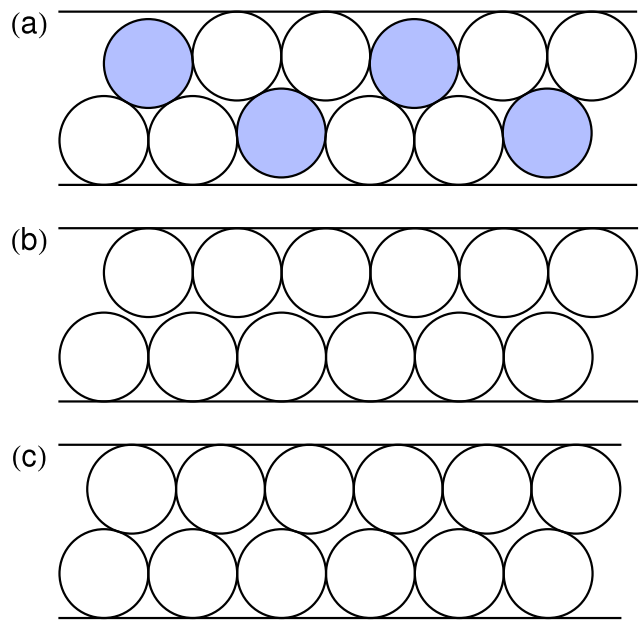

FIG. 2: (Color online) (a) Configuration of disks at the maximum possible packing fraction $\phi_{\max} \simeq 0.8074$, when $H_d = 1.95\,\sigma$. The light blue disks do not touch the sides of the channel. (b) Configuration of the disks at a density $\phi_K \simeq 0.8054$. This is the highest-density state that can be reached if all disks are in contact with the channel walls. It is not a jammed state as the disks in the upper row can be translated with respect to those in the lower row. (c) Also a configuration at ϕ_K but at the limit of the translation of the upper row to the left.

key feature for producing glassy behavior, so perhaps it is not surprising that the presence of NNN contacts introduces features that are absent in the narrower channel which has only NN contacts.

In the NN model, the dynamics becomes activated around a packing fraction $\phi_d > 0.48$ [1–5]. This is due to the onset of caging, a feature connected with the growth of a particular structural feature, zigzag order [1, 2]. Zigzag order (see Eq. (36) for its definition) can be regarded as a form of bond-orientational order. Accompanying this activated dynamics are many of the other features which one associates with glasses, such as the appearance of a plateau in time dependent correlation functions, dynamic heterogeneities, etc. [2, 3]. We expect there to be very similar behavior in the NNN model, but that is not the focus of this paper. Instead our interest is in a feature which occurs *only* in the NNN model, at a packing fraction $\phi_K \simeq 0.8054$. (The maximum packing fraction for $H_d = 1.95\,\sigma$ is $\phi_{\max} \simeq 0.8074$; see Fig. 2(a).) The phenomenology of this feature turns out to be very similar to that of the ideal glass transition [6].

There are standard arguments against there being any genuine phase transition in one dimension [7] which we expect will apply to our narrow channel problem, and will rule out any genuine phase transition at finite pressure. The ideal glass transition of hard spheres in three dimensions is estimated to occur at a ϕ_K of around 0.62 [6]; the analogue of the dynamical transition at ϕ_d is around 0.58. In two dimensions, activated dynamics has been observed to set in at around $\phi_d \simeq 0.78$ in binary [8] and weakly polydisperse [9] mixtures of hard disks and the ideal glass transition is estimated to occur at a packing fraction $\phi_K \simeq 0.81$ [6]. It is usually believed that the dynamical transition at ϕ_d is avoided in any finite dimension and it is uncertain whether the transition found at ϕ_K in an approximate treatment, valid for dimension $d \to \infty$, will survive to lower dimensions. These approximate calculations involve the analogue of one-step replica symmetry breaking, which may be destroyed by fluctuation effects in any physically interesting dimension [10, 11]. Thus while the absence of a genuine phase transition in our channel system is not surprising, it is possible that glass transitions in two or three dimensions might also be avoided.

A piece of evidence that the feature at ϕ_K might be the remnant of the ideal glass transition is from the growth of a particular correlation length, which grows to its maximum value (around $15\,\sigma$) at ϕ_K and then falls. We shall explain in Sec. VIII that this length, which we call the shear-penetration length ξ_3, is the distance over which a shear displacement of the two rows of disks decreases with distance from an amorphous boundary. It is very similar in nature to the penetration length for amorphous order calculated by molecular dynamics in Refs. [12, 13]. The penetration length can be defined in equilibrium (like our ξ_3) and is conceptually simpler than the point-to-set length scale [14, 15], which is the length scale below which ergodicity is broken in a region of fluid with amorphous boundaries; but both of these length scales are expected to diverge at the glass transition [16]. In three dimensions, the largest values found for the penetration length to date are smaller than those we can find in our system, so in this sense we have in our model better evidence for the ideal glass transition than has been found in three dimensions.

The second aspect of our feature at ϕ_K which makes us identify it as an avoided ideal glass transition is that the α-relaxation time τ_α, which we estimate using the ideas in Ref. [1], will appear to diverge in a Vogel–Fulcher manner,

$$\tau \sim \exp\left(\frac{\text{const.}}{\phi_K - \phi}\right), \tag{1}$$

which is of the form expected for behavior near the ideal glass transition. Because there is no real singularity at ϕ_K as the transition is avoided, the time scales will not truly diverge there and will in fact diverge only for $\phi \to \phi_{\max}$.

There is a long tradition in the theory of glasses of attributing glass behavior to the growth of particular types of structural order, such as icosahedral order in three

dimensions [17–19]. Recent work by Cubuk et al. [20] on the flow of jammed and glassy systems under stress has shown that regions that are susceptible to rearrangement can be discovered by machine-learning methods that combine information derived from several features of the local structure, such as the radial distribution of particles and the bond angles. Since our narrow-channel system with NNN contacts is relatively simple, we are able to identify the collective motions of the disks that lead to the apparent ideal glass behaviors. Thus the onset of slow dynamics near ϕ_d we can identify with the growth of bond-orientational order. The feature at ϕ_K which seems related to the ideal glass transition is connected with the growth of crystal-like order. We shall discuss this matter in detail in Sec. VIII. In the limit of very wide channels, when a real transition can arise rather than just an avoided transition, the feature at ϕ_d becomes, we suspect, the fluid–hexatic transition, and the feature at ϕ_K evolves to be the hexatic–crystal transition. The length scale ξ_3 appears to be similar to the penetration length for amorphous order studied in the glass community. For a system of disks in a channel of any length, work must be done to displace one disk along the channel, relative to its nearest neighbors. But in a short channel with length $L < \xi_3$, displacing one disk will cause the displacement of all of the disks of one row relative to the other row, as shown in Fig. 2(c). This rigidity for $L < \xi_3$ is like that of an amorphous solid.

Another example of the utility of the NNN channel problem for the study of glasses is the work of Ashwin and Bowles [21]. They determined exactly the number $N_c(\phi)$ of jammed states at packing fraction ϕ and calculated from it the complexity $S_c(\phi) = [\ln N_c(\phi)]/N$. They found an apparent kink in $S_c(\phi)$ at a packing fraction 0.8064, a density which we shall call $\phi_{\rm rcp}$, above which $S_c(\phi)$ decreases rapidly to zero. The jammed states which exist above this density contain increasing amounts of the buckled-crystal ordering seen in Fig. 2(a). It is this feature which makes it natural to identify the kink in $S_c(\phi)$ with random close packing, which for hard spheres in three dimensions occurs at a packing fraction close to 0.64 [22]: jammed states with $\phi > 0.64$ are known to contain increasing amounts of face-centered cubic crystal ordering [23]. Ashwin and Bowles also found that using the Lubachevsky–Stillinger algorithm [24] to find jammed states always led to a jammed state with a packing fraction close to $\phi_{\rm rcp}$ if one started from a high enough initial density. Observe that in our NNN channel system $\phi_{\rm max} \simeq 0.8074$, $\phi_K \simeq 0.8054$, and $\phi_{\rm rcp} \simeq 0.8064$, which are rather close to each other, compared to their corresponding values in three dimensions. These numerical values are for $H_d = 1.95\,\sigma$. The general formulas are $\phi_K = \pi\sigma/(2H_d)$ and $\phi_{\rm max} = 3\pi\sigma^2/(2H_d\,a)$, where

$$a = \sigma + 2[\sigma^2 - (h - \sqrt{3}\,\sigma/2)^2]^{1/2} \qquad (2)$$

is the length of one unit cell of the buckled crystal; $\phi_{\rm rcp}$ has been estimated only for $H_d = 1.95\,\sigma$ [21]. Notice that $\phi_{\rm max}$ coincides with ϕ_K when $h = \sqrt{3}\,\sigma/2$ and that the difference between them increases as H_d increases.

From the results of simulations in three dimensions, it has been noted [25, 26] that the rate at which distinct, disordered states disappear with increasing density has a sharp maximum at a particular density. This maximum becomes narrower for larger system sizes, perhaps becoming infinitely sharp and leading to a well-defined $\phi_{\rm rcp}$ in the thermodynamic limit [25]. Kamien and Liu [26] argue that such a feature, which corresponds to a discontinuity in $S_c(\phi)$, will be accompanied by a divergence of the pressure on a metastable branch of the equation of state. They suggest that the position of this singularity may be obtained by extrapolation from the low-density portion of the equilibrium equation of state. We suspect that in our equilibrium calculation, the apparent divergence of the force F, when extrapolated to ϕ_K, might have some connection with their argument. It should be noted, however, that the equilibrium state at ϕ_K is certainly not jammed and that a snapshot of it would show much more disorder than in Fig. 2(b), with disks at random distances from the walls. (This can be deduced from the density profile discussed later in Sec. III and illustrated in Fig. 7.) Using such a configuration as the starting point for the Lubachevsky–Stillinger algorithm [24] will always result in a slightly denser state, quite possibly one with packing fraction close to $\phi_{\rm rcp}$. An interesting discussion of possible singularities in the metastable fluid branch of the hard sphere fluid is given in Ref. [27].

The plan of the paper is as follows. In Sec. II we set up the transfer matrix formalism for the NNN channel problem. It is more intricate than that for the NN case and is harder to solve numerically, especially for large packing fractions. In Sec. III we study the equation of state and show that the pressure apparently diverges when ϕ is extrapolated to ϕ_K. We also obtain the local density variation across the channel. As the packing fraction increases, the disks are pushed more and more against the channel walls, but for $\phi \sim \phi_K$ some of the disks lift away from the walls in order to achieve the buckled crystalline state of Fig. 2(a). In Sec. IV we obtain from the eigenvalues of the transfer matrix three of the correlation lengths: the length scales for zigzag and buckled-crystal order (ξ_{zz} and ξ_c), and the shear penetration length ξ_3. In Sec. V we describe the distribution functions for the longitudinal separation of nearest- and next-nearest-neighbor disks. From these we can obtain the variances of these separations, which are used in Sec. VI to understand the variation of ξ_3 with F, the longitudinal force applied to the system. In Sec. VII we use the transfer matrix formalism to describe how the system evolves towards the crystalline state as $\phi \to \phi_{\rm max}$. Finally in Sec. VIII we further discuss the shear penetration length ξ_3 and explain why the α-relaxation time might be expected to show an apparent divergence at ϕ_K.

II. MODEL AND TRANSFER INTEGRAL EQUATION

In this section we set up the transfer matrix formalism for disks in a channel that is wide enough to allow contact between next-nearest neighbors. Because a disk cannot overlap its nearest neighbors, it is convenient to reparametrize the configuration not in terms of $\{x_i, y_i\}$ but rather in terms of horizontal separations s_i, defined by

$$s_1 \equiv x_1 \quad \text{and} \quad s_i \equiv x_i - x_{i-1} - \sigma_{i,i-1} \quad \text{for } i \geq 2\,, \tag{3}$$

where

$$\sigma_{i,j} \equiv \left(\sigma^2 - [y_i - y_j]^2\right)^{1/2}. \tag{4}$$

Notice that when the disks touch, $s_i = 0$.

In terms of the variables $\{s_i, y_i\}$, the configuration integral can be written

$$\begin{aligned} &Q(N,L) \\ &\quad = \prod_{i=1}^{N} \int_0^\infty ds_i \int dy_i \\ &\qquad \times \theta\bigl(L - \textstyle\sum_{j=1}^{N} s_j - \sum_{j=1}^{N-1} \sigma_{j,j+1}\bigr) \prod_{k=2}^{N-1} \Theta_k\,, \end{aligned} \tag{5}$$

where $\theta(x)$ is the Heaviside step function and

$$\Theta_k = \theta(s_k + s_{k+1} + \sigma_{k,k+1} + \sigma_{k,k-1} - \sigma_{k-1,k+1})\,. \tag{6}$$

In Eq. (5), the variables y_i are integrated over the range $[-h/2, h/2]$; the same limits will be assumed in later expressions that involve y-integrations. Note that the first step function in (5) imposes the constraint $x_N \leq L$ and the remaining step functions exclude configurations in which next-nearest-neighbor disks overlap. A variant of our model which is periodic in the y-direction has been studied in Ref. [28].

It is inconvenient to work in an ensemble in which the length L is constant, though this was the approach taken by Barker [29]. Instead we follow Kofke and Post [30] in transforming to an ensemble in which the longitudinal force, F, is constant. This amounts to taking the Laplace transform of (5) with respect to L,

$$\begin{aligned} &\hat{Q}(\beta F,N) \\ &\quad = \int_0^\infty e^{-\beta F L}\, Q(L,N)\, dL \\ &\quad = \frac{1}{\beta F} \prod_{i=1}^{N} \int_0^\infty ds_i\, e^{-\beta F s_i} \int dy_i \\ &\qquad \times e^{-\beta F \sum_{j=1}^{N-1} \sigma_{j,j+1}} \prod_{k=2}^{N-1} \Theta_k\,, \end{aligned} \tag{7}$$

where $\beta = 1/k_B T$. Equation (7) agrees with the results of Kofke and Post [30] and Varga et al. [31] who considered only the case $h/\sigma \leq \sqrt{3}/2$ in developing their transfer matrix formalism: in that special case, the step functions are all unity, because $\sigma_{k,k+1} + \sigma_{k,k-1} \geq \sigma_{k-1,k+1}$; the s_i-integrations can be completed analytically, giving

$$\hat{Q}(\beta F, N) = \frac{1}{(\beta F)^{N+1}} \prod_{i=1}^{N} \int dy_i\, e^{-\beta F \sum_{j=1}^{N-1} \sigma_{j,j+1}}\,. \tag{8}$$

In this paper, we shall be concerned mainly with the case $h/\sigma > \sqrt{3}/2$, so that we cannot make use of the simplification (8).

A. Formulation of an integral equation

In (7), the integrals over $\{s_i, y_i\}$ can be performed one at a time. We write

$$\begin{aligned} &\hat{Q}(\beta F, N) \\ &\quad = \frac{1}{\beta F} \int_0^\infty ds_N \int dy_N \int dy_{N-1}\, q_N(y_N, y_{N-1}, s_N)\,, \end{aligned} \tag{9}$$

where the function q_N can be calculated iteratively, starting from

$$q_2(y_2, y_1, s_2) = \frac{1}{\beta F}\, e^{-\beta F(s_2 + \sigma_{2,1})}\,. \tag{10}$$

Subsequent functions q_k (with $k = 3$ to N) are given by

$$\begin{aligned} &q_{k+1}(y_{k+1}, y_k, s_{k+1}) \\ &\quad = e^{-\beta F(s_{k+1} + \sigma_{k+1,k})} \\ &\qquad \times \int_0^\infty ds_k \int dy_{k-1}\, \Theta_k\, q_k(y_k, y_{k-1}, s_k)\,. \end{aligned} \tag{11}$$

For $k \gg 1$, the form of the function q_k approaches that of the nodeless eigenfunction corresponding to the largest eigenvalue λ_1 of the integral equation

$$\begin{aligned} &\lambda_n\, u_n(y_2, y_1, s_2) \\ &\quad = e^{-\beta F(s_2 + \sigma_{2,1})} \int_0^\infty ds_1 \int dy_0\, \Theta_1\, u_n(y_1, y_0, s_1)\,, \end{aligned} \tag{12}$$

so that

$$q_k(y_k, y_{k-1}, s_k) \approx A \lambda_1^k u_1(y_k, y_{k-1}, s_k)\,, \tag{13}$$

where A is a constant, independent of k. Accordingly, the free energy $\Phi(\beta F, N)$ derived from the partition function $\hat{Q}(\beta F, N) \sim \lambda_1^N$ is given by

$$\beta\Phi(\beta F, N) = -\ln \hat{Q}(\beta F, N) = -N \ln \lambda_1 + \mathrm{O}(1)\,. \tag{14}$$

This free energy is essentially [32] the Gibbs free energy with respect to the longitudinal force F, so that

$$L = \frac{\partial \Phi}{\partial F} = -\frac{N}{\beta \lambda_1} \frac{\partial \lambda_1}{\partial F} \,, \tag{15}$$

but it is also (via the dependence on the channel width) of the Helmholtz type with respect the transverse force F_T,

$$F_T = -\frac{\partial \Phi}{\partial h} = \frac{N}{\beta \lambda_1} \frac{\partial \lambda_1}{\partial h} \,. \tag{16}$$

We are aware of no simple, general relationship between F and F_T; in particular, the stress tensor cannot be assumed to be isotropic.

It is of interest to see how the integral equation of Ref. [30] arises from (12) when $h/\sigma \le \sqrt{3}/2$. For that case, the step function Θ_1 in (12) is always unity, so that the dependence on s_2 reduces to $u_n(y_2, y_1, s_2) = \exp[-\beta F s_2]\, u_n(y_2, y_1, 0)$. By using this form in (12) and integrating both sides with respect to y_1, we obtain

$$\beta F \lambda_n \, \phi_n(y_2) = \int e^{-\beta F \sigma_{2,1}} \, \phi_n(y_1) \, dy_1 \,, \tag{17}$$

where $\phi_n(y_1) = \int u_n(y_1, y_0, 0)\, dy_0$. The one-dimensional integral equation (17) is of the form derived by Kofke and Post [30], with eigenvalue $\beta F \lambda_n$.

B. Properties of the integral equation

The integral equation (12) has the same form when all the y-coordinates are reversed in sign. Each solution consequently has either even or odd parity, $u_n(-y_2, -y_1, s) = \pm u_n(y_2, y_1, s)$, corresponding to the parity of the solutions of Kofke and Post's integral equation for the case of nearest-neighbor interactions.

By using the symmetry of the function Θ_1 under interchange of (y_2, s_2) with (y_0, s_1), it is straightforwardly shown that real eigenfunctions u_n and u_m corresponding to different real eigenvalues λ_n and λ_m are orthogonal, in the sense that the bilinear form

$$B[u_n, u_m] \equiv \int_0^\infty ds \int dy_1 \int dy_2 \, e^{\beta F (s + \sigma_{1,2})} \times u_n(y_1, y_2, s)\, u_m(y_2, y_1, s) \tag{18}$$

equals zero for $\lambda_n \ne \lambda_m$. This integral always converges because, from (12), both eigenfunctions decrease as $\exp[-\beta F s]$ for large s. Equation (12) can also have complex eigenvalues, which occur in complex conjugate pairs: the corresponding eigenfunctions u_n and $u_{n+1} \equiv u_n^*$ satisfy $B[u_n, u_{n+1}] = 0$ and are also orthogonal to the real eigenfunctions. These complex solutions are used later in Sec. VII, in a calculation of the correlation length at high density.

The orthogonality relation can be used to determine the coefficient A in Eq. (13). Assuming that the function q_2 can be expanded in terms of the eigenfunctions u_n,

$$q_2 = A \lambda_1^2 u_1 + \sum_{n>1} c_n u_n \,, \tag{19}$$

projection of both sides onto the eigenfunction u_1 gives the exact relation

$$\begin{aligned} B[u_1, q_2] &= \frac{1}{\beta F} \int_0^\infty ds \int dy_1 \int dy_2 \, u_1(y_1, y_2, s) \\ &= A \lambda_1^2 \, B[u_1, u_1] \,, \end{aligned} \tag{20}$$

which will be of use later, in Sec. II C.

The eigenvalue problem can also be formulated variationally. The eigenvalues are stationary points of the functional

$$\Lambda[u] = \frac{K[u,u]}{B[u,u]} \,, \tag{21}$$

where

$$K[u,v] = \int_0^\infty ds_1 \int_0^\infty ds_2 \int dy_0 \int dy_1 \int dy_2 \times u(y_1, y_2, s_2)\, \Theta_1 \, v(y_1, y_0, s_1) \,. \tag{22}$$

This stationary property of the functional Λ can be verified by evaluating the functional derivative $\delta\Lambda/\delta u$ at $u = u_n$, making use of the eigenvalue equation (12) satisfied by u_n.

The variational formulation of the eigenvalue problem can be used to obtain the length of the system, by using (15) in the form

$$\beta L/N = -\frac{\partial}{\partial F} \ln \Lambda[u_1] \,. \tag{23}$$

The functional Λ depends on F explicitly via the factor $\exp[\beta F(s + \sigma_{1,2})]$ and implicitly via the eigenfunction u_1. Terms in (23) that arise from the F-dependence of u_1 vanish, owing to the variational property of Λ, leaving

$$L/N = \int_0^\infty ds \int dy_1 \int dy_2 \, (s + \sigma_{1,2}) \, e^{\beta F (s + \sigma_{1,2})} u_1(y_1, y_2, s)\, u_1(y_2, y_1, s) / B[u_1, u_1] \,, \tag{24}$$

which is analogous to Eq. (2.12) of Ref. [30]. The form of the last expression strongly suggests that

$$\rho(y_1, y_2, s) \equiv e^{\beta F(s+\sigma_{1,2})} u_1(y_1, y_2, s) \times u_1(y_2, y_1, s)/B[u_1, u_1] \tag{25}$$

is the equilibrium distribution function for the horizontal separation and y-coordinates of a neighboring pair of disks. This identification will be verified directly in the following section. In a similar way, the variational principle can be used to derive a wall contact theorem [33, 34] for the transverse force,

$$\beta F_T/N = \frac{\partial}{\partial h} \ln \Lambda[u_1] = \rho_1(h/2)\,, \tag{26}$$

where $\rho_1(y)$ is the probability density for a disk to have its center at y:

$$\rho_1(y) = \int_0^\infty ds \int dy_2\, \rho(y, y_2, s)\,. \tag{27}$$

C. Distribution functions

The probability distribution $\rho_k(y_k, y_{k-1}, s_k)$ for neighboring disks $k-1$ and k to be found at separation s_k with y-coordinates y_{k-1} and y_k can be derived systematically by performing all of the integrals in (7) except those for s_k, y_{k-1} and y_k. The integrals over variables s_l and y_{l-1} for $l < k$ give a factor of $q_k(y_k, y_{k-1}, s_k)$ and those for s_l and y_l for $l > k$ give a factor of $q_{N-k+2}(y_{k-1}, y_k, s_k)$. The normalized result for ρ_k is

$$\rho_k(y_k, y_{k-1}, s_k) = q_k(y_k, y_{k-1}, s_k)\, q_{N-k+2}(y_{k-1}, y_k, s_k)\, e^{\beta F(s_k+\sigma_{k,k-1})}/\hat{Q}(\beta F, N)\,. \tag{28}$$

For the special case $k = N$, use of (10) shows that (28) reduces correctly to $q_N(y_N, y_{N-1}, s_N)/\beta F\hat{Q}(\beta F, N)$, which is normalized to unity.

In the thermodynamic limit $N \gg 1$, most of the disks k are far from both ends of the system, so that $k \gg 1$ and $N - k \gg 1$. We can make the approximation (13) for q_k, q_{N-k+2}, and q_N, giving

$$\rho_k \to \rho(y_k, y_{k-1}, s_k) = \beta F A \lambda_1^2 \frac{u_1(y_k, y_{k-1}, s_k)\, u_1(y_{k-1}, y_k, s_k)\, e^{\beta F(s_k+\sigma_{k,k-1})}}{\int_0^\infty ds_N \int dy_N \int dy_{N-1}\, u_1(y_N, y_{N-1}, s_N)}\,, \tag{29}$$

which, by using the result (20), is equivalent to (25).

D. Numerical solution of the integral equation

We solve the integral equation (12) by discretization, approximating the integrals by sums. This converts (12) into a matrix eigenvalue problem

$$\lambda \mathbf{u} = \mathsf{M}\mathbf{u}\,, \tag{30}$$

in which the matrix M is dense and nonsymmetric. For large values of F, the eigenfunctions are large when y_1 and y_2 lie within a distance ϵ of the walls $y = \pm h/2$, where

$$\epsilon = h - \sqrt{3}\,\sigma/2\,. \tag{31}$$

It is important to treat these regions accurately without increasing the dimension of M unnecessarily. To achieve this, we make a change of variables

$$y(t) = at + b\tanh[ct]\,, \tag{32}$$

where $y(\pm 1) = \pm h/2$ and the values of t are uniformly spaced in the interval $[-1, 1]$. The positive parameters a, b, and c are chosen so that approximately two thirds of the values of y given by (32) lie within a distance ϵ of the walls and are nearly uniformly spaced within these narrow regions.

For simplicity, the eigenfunctions $u_n(y_2, y_1, s)$ are tabulated at equal intervals in s. For any specified values of y_2 and y_1, there is a value of s (call it $s_{\max}(y_2, y_1)$) beyond which the eigenfunctions $u_n(y_2, y_1, s)$ decrease as $\exp[-\beta F s]$. The portion of the s integration with $s > s_{\max}$ can be completed analytically, so that there is no need to tabulate u_n beyond this point; this helps to reduce the dimension of the eigenvalue problem. Elsewhere, the integrands are linearly interpolated from their tabulated values.

Even with the y transformation and the treatment of the s integration discussed above, the matrix M in Eq. (30) is still too large to be stored in computer memory, so that the eigenvalue problem must be solved by an iterative method. (With 100 points for each of y_1, y_2, and s, M is a $10^6 \times 10^6$ matrix. With fewer points we have found it hard to capture accurately the rapid variation of

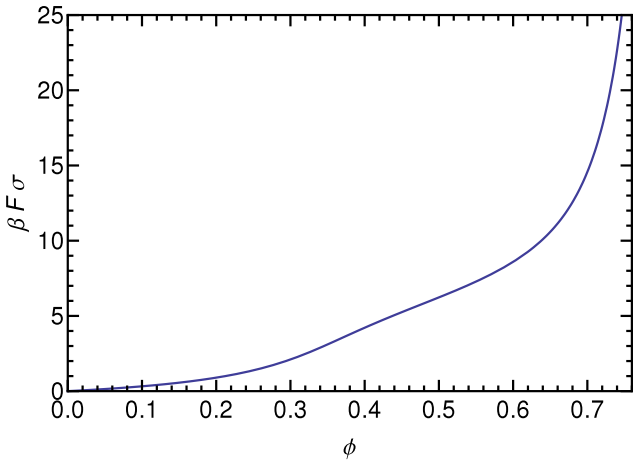

FIG. 3: (Color online) Equation of state: $\beta F\sigma$ as a function of packing fraction ϕ, for hard disks of radius σ in a channel of width $H_d = 1.95\,\sigma$.

the eigenfunctions near the wall, as is visible in Fig. 7.) Simple iteration of (12) is adequate for finding the first two real eigenfunctions, provided the process starts with a function of the appropriate parity. When more eigenfunctions are required, we find it convenient to use the ARPACK subroutine library [35], which implements the iterative method due to Arnoldi [36].

To test our numerical methods, we have used them to calculate the equation of state and the correlation length ξ for a system of disks in a narrow channel with $h = \sqrt{3}\,\sigma/2$. For this case in which NNN disks do not interact, these quantities are more easily found by solving the one-dimensional integral equation (17) [1, 30], which leads to a much smaller (and symmetric) transfer matrix. Results from the two approaches are in excellent agreement and give us some confidence in the reliability of our later results for the case $h = 0.95\,\sigma$.

III. EQUATION OF STATE

The equation of state is central to the study of fluids. From it one can determine the phase diagram. Equation (24) gives L/N in terms of the F-dependent eigenfunction $u_1(y_2, y_1, s)$, and so determines the equation of state; that is, the relation between F and the packing fraction ϕ, where

$$\phi \equiv \frac{N\pi\sigma^2}{4LH_d}\,. \tag{33}$$

The equation of state is shown in Fig. 3, for moderate values of F and $h = 0.95\,\sigma$. Notice the shoulder near $\phi \simeq 0.5$: this is due to the onset of zigzag order [1]. If one could study progressively wider channels we believe that this shoulder would evolve into the feature seen in the equation of state of a two-dimensional fluid for $\phi \simeq 0.71$, which is the transition between the fluid and hexatic and crystal transitions [37]. We expect that if one could study the compressibility for a range of channel widths it would have a peak at the shoulder which would evolve into the singularity seen in the infinite system in Ref. [37, 38]. This is reminiscent of what happens in (say) strips $n \times \infty$ of the two-dimensional Ising ferromagnet: the peak in the specific heat for finite n evolves into a divergence at criticality as $n \to \infty$ [39].

In Figs. 4 and 5 we compare the longitudinal and transverse pressures $P_{xx} = F/h$ and $P_{yy} = F_T/L$ calculated for the NN and NNN models with the equation of state of a system of disks in two dimensions, simulated by molecular dynamics [37]. Notice that at very low densities or packing fractions, Figs. 4 and 5 show that the equation of state approaches that of the two-dimensional system, which is isotropic: $P_{xx} = P_{yy}$. However, as the packing fraction increases beyond about 0.1, the system becomes sensitive to its channel structure. For wider channels, the approximate equality of P_{xx} and P_{yy} for small ϕ should extend to higher packing fractions, but probably not in any smooth way because of layering effects. It can be observed also that for the wider channel studied in Fig. 5, the results are closer overall to those of the full two-dimensional system than those for the narrower system displayed in Fig. 4.

The force F becomes large for $\phi \to \phi_{\max}$, the density of the most closely packed jammed state, which is the buckled crystal identified in Ref. [21] and shown in Fig. 2(a). From the general arguments of Salsburg and Wood [40], we might expect to find

$$\beta F \simeq \frac{d_{\rm eff} N}{L(1-\phi/\phi_{\max})} \tag{34}$$

as ϕ approaches $\phi_{\max}$, with $d_{\rm eff} = d = 2$. This form for the equation of state can also be obtained from the high-density limit of the integral equation (12), as discussed in Sec. VII. It is therefore of interest to consider $1/F$ as a function of ϕ, as shown in Fig. 6. This shows a linear dependence on ϕ over a range of ϕ, extrapolating to zero at $\phi \simeq 0.8054$, which is *not* the maximum density of the buckled crystal. Instead, the data in Fig. 6 is consistent with the equation

$$\beta F \simeq \frac{d_{\rm eff} N}{L(1-\phi/\phi_K)}, \tag{35}$$

with an effective dimensionality $d_{\rm eff} \simeq 0.91$, at least for the data that lies close to the straight line. There is no actual divergence of F as $\phi \to \phi_K$, as the data points in the vicinity of ϕ_K do not lie on the straight line. The only true divergence in F is at the largest possible value of ϕ, $\phi_{\max} \simeq 0.8074$, which is the packing fraction of the buckled crystal. Our finding $d_{\rm eff} \neq d$ has a counterpart in the case of three-dimensional hard spheres [41], where $d_{\rm eff} \simeq 2.53$ rather than 3. Notice that our $d_{\rm eff}$

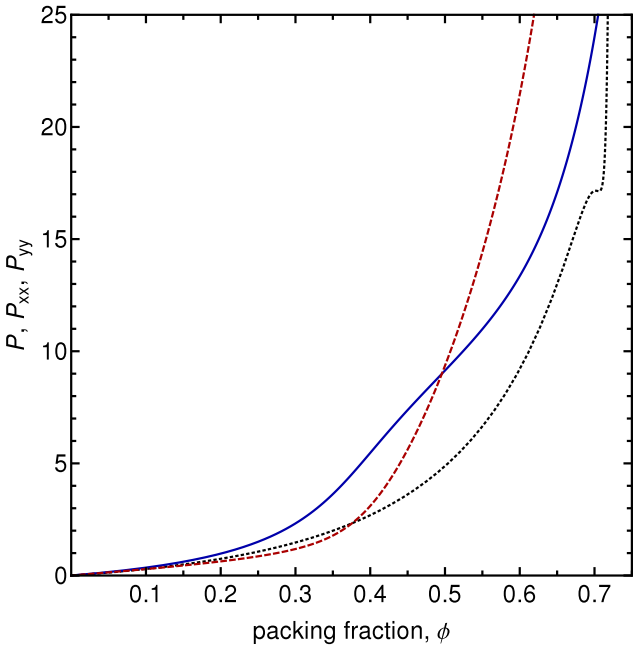

FIG. 4: (Color online) Equation of state: P, scaled to $\beta P\sigma^2$, as a function of packing fraction ϕ, for hard disks of radius σ in a channel of width $h = \sqrt{3}\,\sigma/2$. Similar results appear in Ref. [31]. Here P_{xx} is the longitudinal pressure F/h (solid blue line), P_{yy} is the transverse pressure F_T/L (red dashed line), and the black dotted line is the simulation results of Kolafa and Rottner [37] on two-dimensional hard disks.

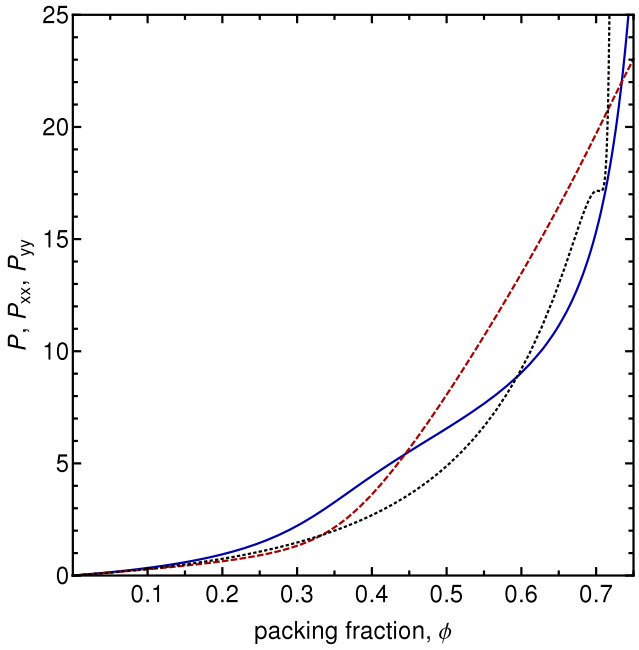

FIG. 5: (Color online) Equation of state: P, scaled to $\beta P\sigma^2$, as a function of packing fraction ϕ, for hard disks of radius σ in a channel with $h = 0.95\,\sigma$. Here P_{xx} is the longitudinal pressure F/h (solid blue line), P_{yy} is the transverse pressure F_T/L (red dashed line), and the black dotted line is the molecular dynamics results of Kolafa and Rottner [37].

is close to 1. This may be because in Fig. 2(b) the top row and the bottom row are partially decoupled so that each behaves like a one-dimensional hard rod gas of maximum density ϕ_K. Each row contains $N/2$ disks which as $\phi \to \phi_K$ will exert a force F_R as for hard rods: $\beta F_R = N/[2L(1-\phi/\phi_K)]$. The combined force exerted by both rows is $F = 2F_R$.

The packing fraction $\phi_K \simeq 0.8054$ at which the force appears to diverge corresponds to the configuration shown in Fig. 2(b). This is not a jammed state as it can be deformed into Fig. 2(c) by sliding the top row of disks to the left. As the density increases above ϕ_K, disks have to move off the wall to fit into the system and the buckled crystal state starts to develop. At all but the highest forces, however, the shaded disks in Fig. 2(a) are only lightly pinched by their neighbors, so that the entropy gained by allowing these disks to be delocalized near the walls overcomes the work that must be done to lengthen the system.

If the apparent singularity in the force at ϕ_K is avoided by an evolution to the buckled state, we should expect to see evidence for this in $\rho_1(y)$, the probability density for finding a disk at y, defined in Eq. (27). In Fig. 7, ρ_1 is plotted as a function of distance from one wall of the channel containing the disk centers. In all cases, the distribution has its maximum at the wall, but a secondary maximum starts to appear for $F > 1000$, and is well developed for $F = 2500$. This secondary maximum clearly corresponds to the trapping of the shaded disks in Fig. 2(a): in the jammed state, the centers of these disks are at a small distance (roughly $0.0840\,\sigma$ for $h = 0.95\,\sigma$) from the walls $y = \pm h/2$ that confine the centers of the disks.

IV. CORRELATION LENGTHS

It is possible to obtain a great many correlation lengths from the ratios of eigenvalues of the transfer integral equation. In our work we focus on three whose interpretation is particularly simple.

The longest correlation length is that associated with the growth of zigzag order or, more precisely, the decay of the correlation between the y-coordinates of well-separated disks i and $i+s$,

$$\langle y_i\, y_{i+s}\rangle \sim (-1)^s \exp(-s/\xi_{zz}), \tag{36}$$

where

$$\xi_{zz} = 1/\ln(\lambda_1/|\lambda_2|)\,. \tag{37}$$

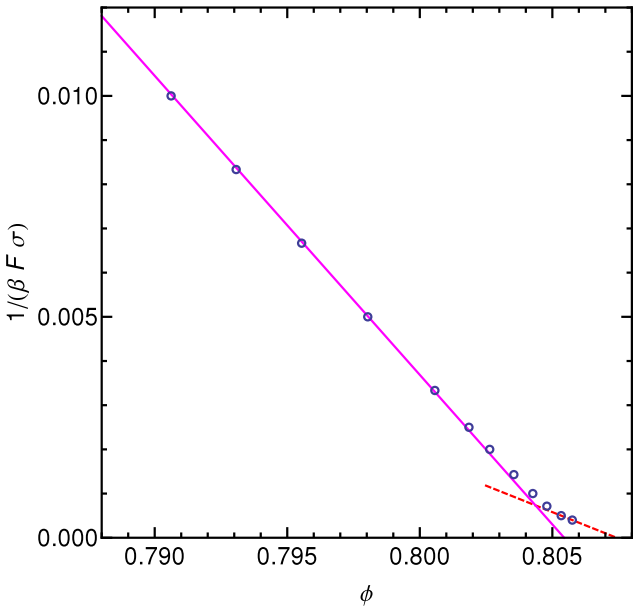

FIG. 6: (Color online) Plot of $(\beta F\sigma)^{-1}$ against packing fraction ϕ for disks in a channel of width $H_d = 1.95\,\sigma$. The circles are our numerical results for $\beta F\sigma \leq 2500$ and the fitted straight solid line extrapolates to zero at $\phi = \phi_K = 0.8054$. The straight dashed line through the last two data points reaches zero at $\phi \simeq 0.8074$, which is approximately $\phi_{\rm max}$. Its gradient corresponds to $d_{\rm eff} = 2.6$ rather than the value 2 expected for $\phi \to \phi_{\rm max}$ [40]. This suggests that the asymptotic regime has not yet been reached and that the plot will level off before approaching zero more steeply with a gradient corresponding to $d_{\rm eff} = 2$. We have been unable to test this prediction by solving the transfer integral equation for $\beta F\sigma > 2500$.

The eigenfunction u_1 is of even parity (it is nodeless) and u_2 has odd parity, so that y has a nonzero matrix element between u_1 and u_2; it may also be noted that the eigenvalues λ_1 and λ_2 have opposite sign. These two features are consistent with the zigzag correlations described by Eq. (36). The F-dependence of the length ξ_{zz} is given in Fig. 8 and is discussed in Sec. VI.

The character of the eigenvalues λ_n for $n > 2$ depends on $\beta F\sigma$. As $\phi \to \phi_{\rm max}$ the next four eigenvalues are two different complex conjugate pairs, as we shall explain in Sec. VII. Outside this limit (and when $\beta F\sigma$ is not small) the first few eigenvalues are real and occur in parity-related doublets of opposite sign, just like λ_1 and λ_2.

A second length scale with a simple interpretation is $\xi_3 = 1/\ln(\lambda_1/|\lambda_3|)$, calculated from the eigenvalues of the first two even-parity eigenfunctions, u_1 and u_3. The functions u_1 and u_3 are depicted in Figs. 9 and 10 for the case $\beta F\sigma = 1000$, for which the correlation length $\xi_3 \simeq 26$. The function u_3 has an approximately planar nodal surface near $s_2 + \sigma_{1,2} = 0.50\,\sigma$, so it is clear that the NN separation $x_2 - x_1$ will have a large matrix element between u_3 and the nodeless function u_1. Accordingly, ξ_3 is the distance over which the nearest-neighbor separations $x_{k+1} - x_k$ remain correlated.

It is shown in Fig. 11 that the correlation length ξ_3 peaks at a value of around 30 for the packing fraction $\phi \approx 0.8049$. Note that our ξ_{zz} and ξ_3 are actually *dimensionless* quantities, as may be seen from Eq. (36), for example. To obtain the physical length scales one has simply to multiply them by L/N. Thus

$$\tilde{\xi}_3 \equiv \xi_3 L/N = \pi\sigma^2/(4H_d\,\phi), \tag{38}$$

where $\tilde{\xi}_3$ is the physical length. When $H_d = 1.95\,\sigma$ and $\phi = 0.8049$, $\tilde{\xi}_3 \approx 0.500\,\xi_3\sigma$. The maximum value of ξ_3 shown in Fig. 11 therefore corresponds to a physical length scale $\tilde{\xi}_3 \approx 15\,\sigma$.

A correlation length that increases to a maximum and then decreases is indicative of an avoided transition. The value of ϕ that corresponds to the peak in ξ_3 is a little less than the value, $\phi_K = 0.8054$, at which $(\beta F\sigma)^{-1}$ appears to approach zero (see Fig. 6). Given that there is no true phase transition at ϕ_K, it is perhaps not surprising that different measures for locating the underlying avoided transition should disagree slightly.

The third length scale, ξ_c, that we have studied is a measure of the extent of buckled-crystal order. For the larger values of $\beta F\sigma$, it can be determined from the ratio $\lambda_1/|\lambda_c|$, where $|\lambda_c|$ is the magnitude of the largest complex conjugate pair of eigenvalues (see Sec. VII). Figure 11 shows that ξ_c grows with increasing $\beta F\sigma$, whilst remaining small in the range of $\beta F\sigma$ that we can study numerically. Its expected behavior for $\phi \to \phi_{\rm max}$ is discussed later, in Sec. VII.

V. PROBABILITY DENSITIES

We have studied the probability density $\rho_{\rm nn}(x_{\rm nn})$ for the centers of neighboring disks to be separated by a distance $x_{\rm nn}$ using

$$\rho_{\rm nn}(x_{\rm nn}) = \int_0^\infty ds \int dy_2 \int dy_1\, \delta(x_{\rm nn} - s - \sigma_{2,1})\rho(y_2, y_1, s). \tag{39}$$

This probability density changes in a striking manner as the packing fraction or force F is increased. Figure 12 shows $\rho_{\rm nn}$ for $\beta F\sigma = 5$, which corresponds to a packing fraction at which zigzag order is starting to develop. For small values of $\beta F\sigma$, the main feature is a cusp at $x_{\rm nn} = \sigma$; but, as zigzag order grows, a broad hump develops at a smaller value of $x_{\rm nn}$: both features may be seen in Fig. 12. Results for larger values of $\beta F\sigma$ are shown in Fig. 13. When $\beta F\sigma = 50$ the cusp at $x_{\rm nn} = \sigma$ has nearly disappeared and would be undetectable on the scale used in Fig. 13. As $\beta F\sigma$ increases further, the position of

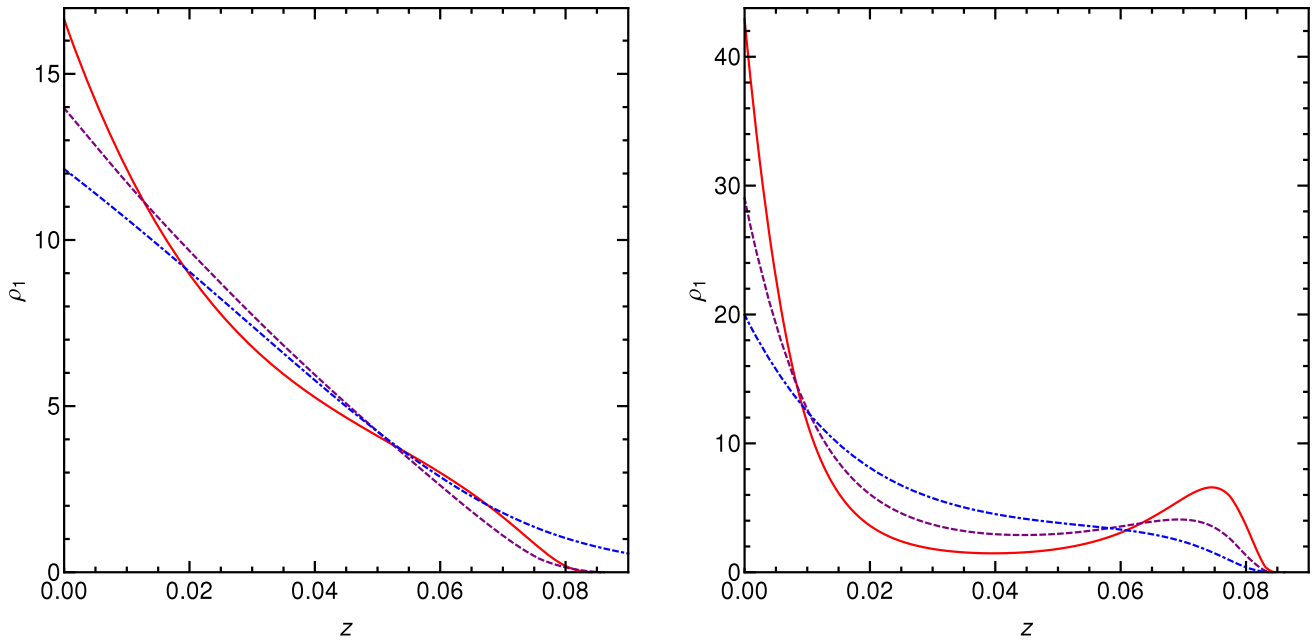

FIG. 7: (Color online) Distribution function $\rho_1\left(\frac{1}{2}h - z\right)$ for the position of a disk in a channel with $h = 0.95\,\sigma$; z is the distance (in units of σ) from one wall of the channel containing the disk centers. On the left the dash-dotted line (blue) denotes $\beta F\sigma = 25$ and $\phi = 0.7431$, the dashed line (purple) $\beta F\sigma = 500$ and $\phi = 0.8025$, and the solid line (red) $\beta F\sigma = 1000$ and $\phi = 0.8042$. The density evolves gradually over this range of F and develops a noticeable shoulder by $\beta F\sigma = 1000$, which anticipates the appearance of a secondary maximum. On the right the dash-dotted line (blue) denotes $\beta F\sigma = 1400$ and $\phi = 0.8047$, the dashed line (purple) $\beta F\sigma = 2000$ and $\phi = 0.8053$, and the solid line (red) $\beta F\sigma = 2500$ and $\phi = 0.8058$. The results show the development of a secondary maximum in the density, as the pressure is increased. At infinite pressure, the center of the trapped disk [shaded in Fig. 2(a)] would be at $z = 0.0840\,\sigma$.

the new peak moves towards the value $x_{\rm nn} \simeq \sigma/2$, as would be expected from Fig. 2(b). For $\beta F\sigma = 100$, the peak is nearly Gaussian in shape and we have directly determined its width by obtaining the variance $\langle (x_{\rm nn} - \langle x_{\rm nn}\rangle)^2\rangle$. The standard deviation of the nearest-neighbor separation is plotted in Fig. 14: it varies as $1/\sqrt{F}$ as $\beta F\sigma$ increases, which is a much slower decrease than would have been naively expected and reflects the ease of sliding the top row with respect to the bottom row in Fig. 2(b).

The separation of next-nearest neighbors has much smaller fluctuations. The variance of $x_{\rm nnn} \equiv (x_{k+2} - x_k)$ is given by

$$\begin{aligned} &\mathrm{var}\, x_{\rm nnn} \\ &\quad = \mathrm{var}([x_{k+2} - x_{k+1}] + [x_{k+1} - x_k]) \\ &\quad = 2\,\mathrm{var}\, x_{\rm nn} + 2\,\mathrm{cov}(x_{k+2} - x_{k+1}, x_{k+1} - x_k)\,. \end{aligned} \tag{40}$$

The covariance term (which is negative) can be obtained from u_1. By following a procedure similar to that described in Sec. II C, it can be shown that

$$\begin{aligned} \langle (x_{k+2} - x_{k+1})(x_{k+1} - x_k)\rangle &= \frac{K[e_1, e_1]}{K[u_1, u_1]} \\ &= \frac{K[e_1, e_1]}{\lambda_1 B[u_1, u_1]}\,, \end{aligned} \tag{41}$$

where $e_1(y_2, y_1, s_2) = (s_2 + \sigma_{2,1})\, u_1(y_2, y_1, s_2)$. The calculation of $\mathrm{var}\, x_{\rm nnn}$ from (40) and (41) thus requires only the distribution of $x_{\rm nn}$ (obtained from u_1) and a single application of the transfer matrix to e_1.

In Fig. 15 the standard deviation of $x_{\rm nnn}$ is plotted for a range of F up to $\beta F\sigma = 2000$. It is close to the expected $1/F$ form, but with some flattening off at the largest values of F. Eventually, the standard deviation must tend to a constant, independent of F, because, as the state of highest density is approached, the NNN separation can have either of two distinct values (see Fig. 2(a)), with fluctuations of order $1/F$ around them.

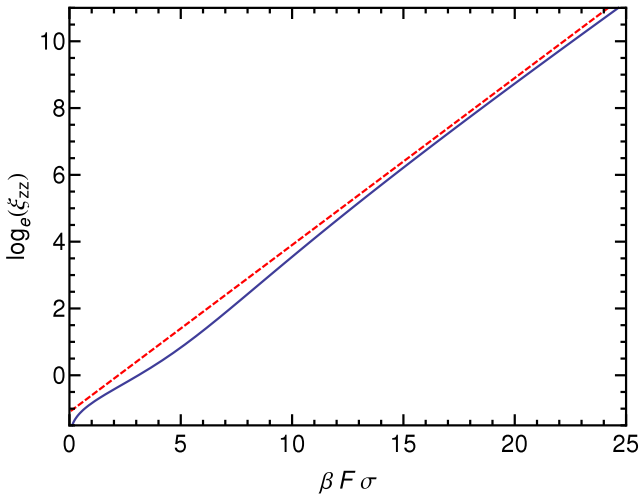

FIG. 8: (Color online) The solid line denotes the correlation length $\xi_{zz} = 1/\ln(\lambda_1/|\lambda_2|)$ derived from the second real eigenvalue λ_2. It is a measure of the growth of zigzag order [see Eq. (36)]. The dashed line is a straight line of gradient 0.5 [see Sec. VI].

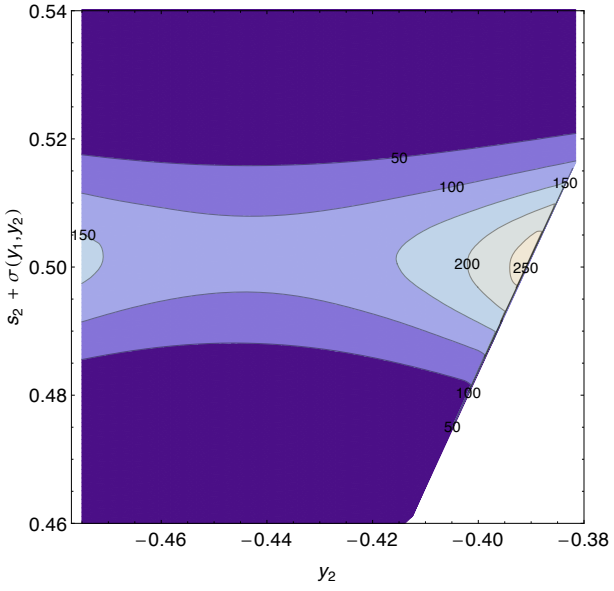

FIG. 9: (Color online) Section through the nodeless eigenfunction $u_1(y_2, y_1, s_2)$ at $y_1 = h/2$, for $h = 0.95\,\sigma$ and $\beta F\sigma = 1000$. The eigenfunction is normalized so that $B[u_1, u_1] = 1$ and has been scaled by $\exp(\beta F[s_2+\sigma_{1,2}]/2)$ for plotting. Distance scales are in units of σ. The white region in the lower right-hand corner corresponds to a disallowed region $s < 0$, in which disks would overlap.

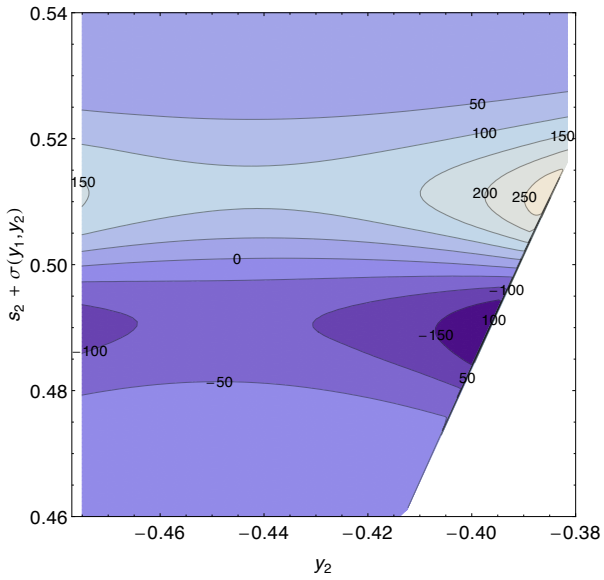

FIG. 10: (Color online) Section through the second even-parity eigenfunction $u_3(y_2, y_1, s_2)$ at $y_1 = h/2$, showing the nodal line at $s_2 + \sigma_{1,2} \simeq 0.50\,\sigma$. The scaling of u_3 is the same as for u_1 in Fig. 9.

VI. UNDERSTANDING THE CORRELATION LENGTHS

There are two important length scales in our problem: the length scale associated with the growth of zigzag or bond-orientational order, ξ_{zz} (see Eq. (36)), and the length scale ξ_3, which describes how the correlations between the nearest-neighbor separations of pairs of disks at numbers k and $k+s$ decay with s,

$$\langle (x_{k+1} - x_k)(x_{k+s+1} - x_{k+s})\rangle_c \sim (-1)^s e^{-s/\xi_3}\,, \qquad (42)$$

where c denotes the cumulant of the correlation. ξ_3 is a measure of the distance along the channel over which the system with $\phi \simeq \phi_K$ comes to resemble Fig. 2(b). We will show later that ξ_3 can also be regarded as the size of a localized thermal fluctuation in which disks of one row are displaced relative to the other row. We have previously obtained ξ_{zz} and ξ_3 from the eigenvalues of the transfer matrix, but in this section we give simple arguments to explain their dependence on F.

In Ref. [1] we were able to give an account of the dependence of ξ_{zz} for the NN model by relating it to the typical distance between defects. For the NNN model, there are many types of defects [21], but we believe the following argument captures the physics of what is going on.

For moderate values of F, typical configurations of the system resemble Fig. 2(b). A pair of defects in this zigzag pattern can be created by removing one disk from the pattern and reinserting it elsewhere, between two disks

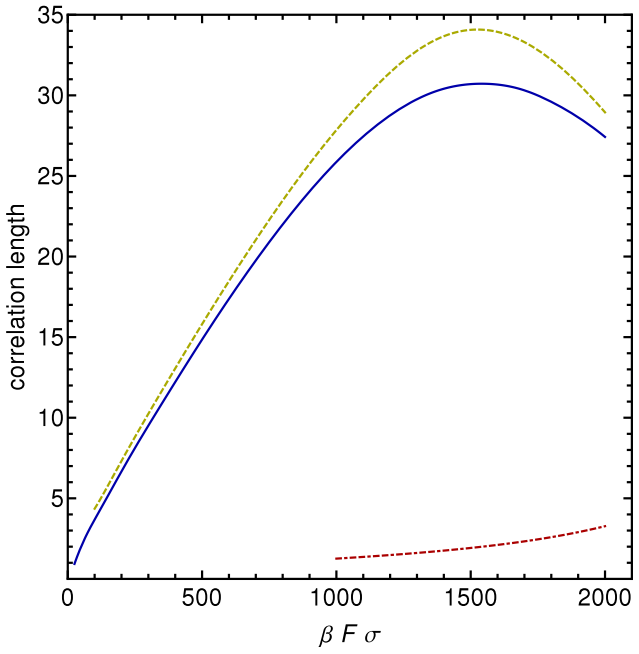

FIG. 11: (Color online) Correlation lengths $\xi_3 = 1/\ln(\lambda_1/|\lambda_3|)$ (solid line) and $\xi_c = 1/\ln(\lambda_1/|\lambda_c|)$ (dash-dotted line), derived from the third real eigenvalue λ_3 and the first complex eigenvalue λ_c. Here ξ_3, which has its greatest value for $\beta F\sigma \approx 1540$ (corresponding to $\phi \approx 0.8049$), is the length scale over which correlations between the separations of nearest-neighbor disks along the x-axis persist. Further, ξ_c describes the persistence of buckled-crystal order; this second length scale grows, but remains small in the range of $\beta F\sigma$ shown. Also shown is the approximation $\xi_3 \simeq 2\,\mathrm{var}\,x_{\mathrm{nnn}}/\,\mathrm{var}\,x_{\mathrm{nn}}$ (dashed line), discussed in Sec. VI.

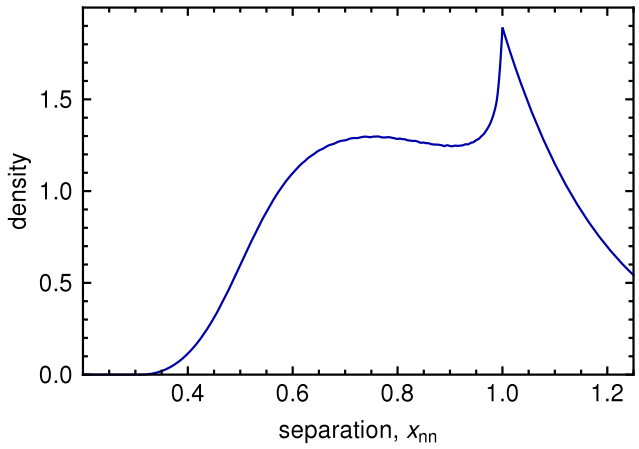

FIG. 12: (Color online) Probability density for the centers of neighboring disks to be separated by distance x_{nn} along the channel, illustrated for $\beta F\sigma = 5$ and $h = 0.95\,\sigma$; x_{nn} is in units of σ. For small F, as shown here, the results are qualitatively similar to those found in [42] for a narrow channel with $h = \sigma\sqrt{3}/2$; the height of the sharp maximum at $x_{\mathrm{nn}} = \sigma$ decreases rapidly with increasing F.

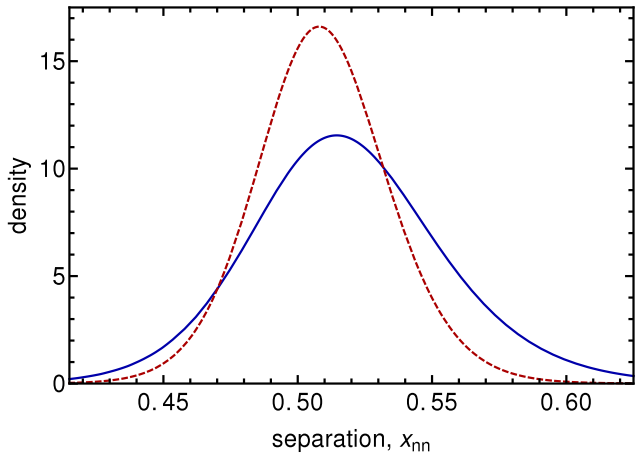

FIG. 13: (Color online) Probability density for the centers of neighboring disks to be separated by distance x_{nn} along a channel with $h = 0.95\,\sigma$, illustrated for $\beta F\sigma = 50$ (solid line) and 100 (dashed line); x_{nn} is in units of σ. As F increases, the distribution approaches the Gaussian form with a variance that decreases as $1/F$.

that lie on the same side of the channel. If the two rows of disks maintain their relative position between the two defects, the increase in length of the system will be σ [43], giving an additional length per defect $\Delta_a \simeq \sigma/2$; the work done to create it will be $F\sigma/2$. We therefore expect the density of defects to vary as $\exp[-\beta F\sigma/2]$ and the correlation length ξ_{zz} to vary as $\exp[\beta F\sigma/2]$, which is the typical spacing of the defects. The dashed line in Fig. 8 shows that this simple argument gives a reasonably good account of the numerical data for $\beta F\sigma < 25$, despite its neglect of any relaxation of the system near the defects. We also note that agreement cannot be maintained indefinitely, as our argument ignores the eventual appearance of buckled crystalline order.

The length scale ξ_3 has no obvious connection with defects, but instead can be understood as an effect due to the accumulation of the random variations in the spacing of NNN disks. To estimate ξ_3, we assume that the coupling of the two rows of disks is weak and that the gaps between next-nearest neighbors are approximately independent random variables, like the gaps between neighbors in a one-dimensional gas of hard rods. With the notation $x_{i,j} \equiv x_i - x_j$ we can write

$$\sum_{k=1}^{m}(-1)^k x_{k+1,k-1} = (-1)^m x_{m+1,m} - x_{1,0}\,. \qquad (43)$$

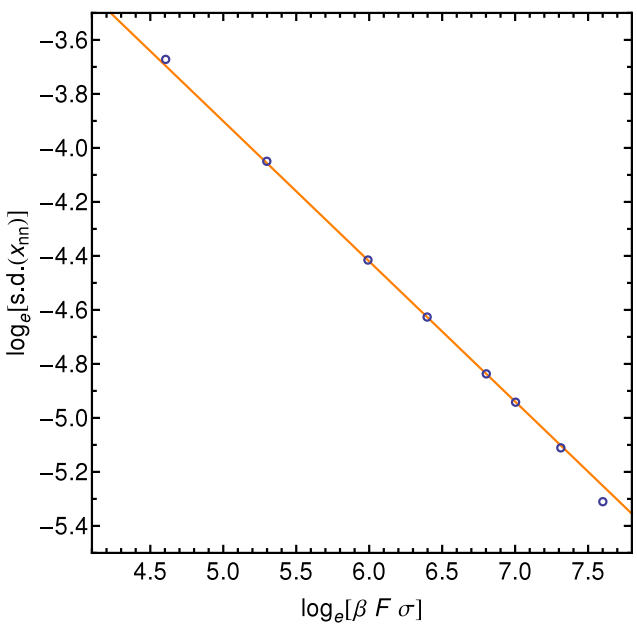

FIG. 14: (Color online) Standard deviation of the nearest-neighbor separation plotted against $\beta F\sigma$; the scales are logarithmic. The solid line has gradient -0.52, showing that the fluctuations in the nearest-neighbor distance decrease approximately as $1/\sqrt{F}$.

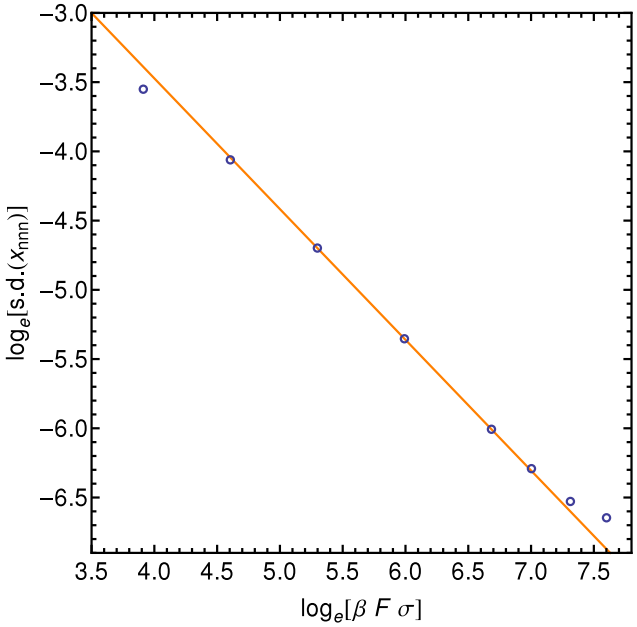

FIG. 15: (Color online) Standard deviation of the separation of next-nearest-neighbor disks plotted against $\beta F\sigma$; the scales are logarithmic. The solid line has gradient -0.94, showing that the fluctuations in the next-nearest-neighbor distance decrease approximately as $1/F$

The left-hand side of this identity is an alternating sum of m next-nearest-neighbor separations: to the extent that these separations are independent random variables, the variance of the left-hand side will grow as $m \operatorname{var} x_{\mathrm{nnn}}$ as m increases. At the same time, the variance of the right-hand side will increase towards $2 \operatorname{var} x_{\mathrm{nn}}$ as the correlation between $x_{m+1,m}$ and $x_{1,0}$ decreases. We therefore expect the correlation to be small when $m \operatorname{var} x_{\mathrm{nnn}} \simeq 2 \operatorname{var} x_{\mathrm{nn}}$. By setting $m = \xi_3$ we obtain the estimate

$$\xi_3 \simeq 2 \, \frac{\operatorname{var} x_{\mathrm{nn}}}{\operatorname{var} x_{\mathrm{nnn}}} . \tag{44}$$

Fig. 11 shows how well this simple formula works. It accounts for both the increase of ξ_3 to its maximum as a function of F as well as its decrease.

The correlation length ξ_3 can also be understood as the typical number of disks that participate in a thermal fluctuation in which a portion of one row moves relative to the other row. The configuration shown in Fig. 2(c) could be regarded as the most extreme fluctuation of this kind: it involves the correlated motion of many disks, and so should be expected to be long-lived on the scale of the collision time. In a localized fluctuation in which m disks of one row are displaced relative to the other, the distances between the disks in one row (averaged over a time that is short compared with the duration of the fluctuation) will change by small amounts of order $\pm\Delta$, with $\Delta \sim (\operatorname{var} x_{\mathrm{nn}})^{1/2}/m$. The total strain energy, which is on the order of the thermal energy $k_B T$, will be approximately

$$m \times \kappa \, \Delta^2 \sim k_B T \, , \tag{45}$$

where the effective spring constant κ for the force conjugate to the next-nearest neighbor separation can be estimated from the fluctuation–response relation

$$\kappa^{-1} = \beta \operatorname{var} x_{\mathrm{nnn}} \, . \tag{46}$$

With our estimate for Δ, Eqs. (45) and (46) lead to $m \sim \xi_3$, where ξ_3 is given by Eq. (44).

VII. BEHAVIOR AS $\phi \to \phi_{\max}$

We have been unable to obtain numerical solutions of the integral equation (12) for very large values of the force, $\beta F\sigma > 2500$. To help fill this gap left by our numerical work, in this section we present an analytical method of solution which is expected to become exact in the limit $\beta F\sigma \to \infty$. We relate the period-six correlations of the buckled crystal to the asymptotic form of the eigenvalues and we calculate the correlation length for crystalline order. We also indicate what features of the eigenfunctions will lead to the high-density form of the equation of state given in Eq. (34).

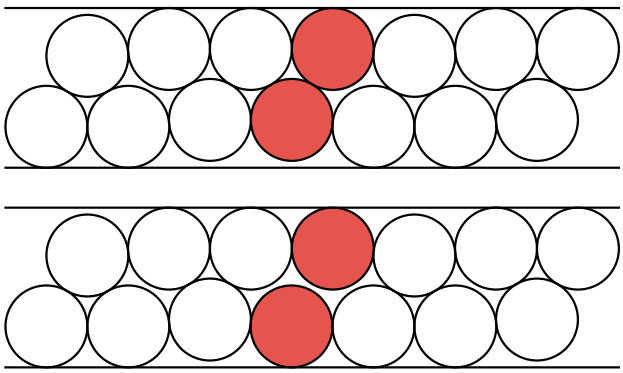

FIG. 16: (Color online) Defects in the high-density buckled-crystal state illustrated in Fig. 2(a). Two distinct types of defect are shown: Each can be created by inserting disks into the buckled crystal at the positions shown (shaded) or at positions related to these by symmetry.

For $F \to \infty$, the system of disks adopts the high-density buckled crystal configuration shown in Fig. 2(a), but for any finite F the crystalline order will be disrupted by the presence of mobile defects. The concentration of these defects will vary as $\exp(-\beta F \Delta_d)$, where Δ_d is the additional length needed to accommodate a defect in the crystal. We therefore expect the mean spacing of defects to increase with F according to

$$\xi_c \sim \exp(\beta F \Delta_d)\,. \tag{47}$$

Our notation for this length scale reflects the fact that ξ_c will also be the distance over which crystalline order persists in the presence of defects.

The shortest (and hence most abundant) defects are of two kinds, illustrated in Fig. 16. Each kind of defect can be created by inserting a pair of disks into the buckled crystal. If six disks, comprising one complete unit cell of length a in the buckled crystal, are removed from a region of perfect crystal, these disks can be reinserted elsewhere in the crystal to create three defects. The net increase in length is

$$3\Delta_d = 3\sigma - a\,, \tag{48}$$

where $a = \sigma + 2\sigma_\epsilon$ and $\sigma_\epsilon = [\sigma^2 - (h - \sigma\sqrt{3}/2)^2]^{1/2}$, so that

$$\Delta_d = \tfrac{2}{3}(\sigma - \sigma_\epsilon)\,. \tag{49}$$

We believe it is worth understanding how the correlation length ξ_c given by (47) and (49) can arise from the integral equation (12) and also how the periodicity of the buckled crystal can be explained. These two matters are very closely connected: the periodicity must appear in the correlation functions, and the dominant contributions to the large-distance correlation functions can be constructed from the eigenfunctions whose eigenvalues are closest in magnitude to the largest eigenvalue λ_1. It follows that there should, for sufficiently large F, be *complex* eigenvalues of (12) whose magnitudes are very similar to λ_1 and whose phases can be related to the periodicity of the buckled crystal. In what follows we show that complex eigenvalues with these properties can be inferred from the form of the integral equation (12).

For sufficiently large F, the solutions of (12) will be sharply peaked near $y = \pm h/2$ and $\pm(\sqrt{3}\,\sigma - h)/2$, with peak widths proportional to $(\beta F)^{-1}$. As seen in Fig. 7, this transverse localization is starting to appear above $\beta F\sigma = 1000$ and it is well developed when $\beta F\sigma = 2500$. But in addition to this localization in y_1 and y_2, the eigenfunctions will also eventually show a similar degree of localization in s_2. In the buckled crystal (see Fig. 2(a)), adjacent disks are either touching, with $s_2 = 0$, or non-touching, with $s_2 = \sigma_\epsilon - \frac{1}{2}\sigma - \sigma_h$, where $\sigma_h = \sqrt{\sigma^2 - h^2}$. In addition to these two separations, the shaded disks in the second of the configurations shown in Fig. 16 are separated by a third distance, $s_2 = \frac{3}{2}\sigma - \sigma_\epsilon - \sigma_h$. This local information regarding pairs of disks can be used to construct an approximate solution of the integral equation.

From the preceding discussion, we expect a solution $u(y_2, y_1, s_2)$ of (12) to have eight narrow peaks with widths $\sim(\beta F)^{-1}$. If u has even parity, there will be only four distinct peak values of u, which we denote by

$$\begin{aligned} v_1 &= u\big(-\tfrac{1}{2}h, \tfrac{1}{2}h, \tfrac{3}{2}\sigma - \sigma_\epsilon - \sigma_h\big) \\ v_2 &= u\big(-\tfrac{1}{2}h, \tfrac{1}{2}h, \sigma_\epsilon - \tfrac{1}{2}\sigma - \sigma_h\big) \\ v_3 &= u\big(-\tfrac{1}{2}h, \tfrac{1}{2}h - \epsilon, 0\big) \\ v_4 &= u\big(-\tfrac{1}{2}h + \epsilon, \tfrac{1}{2}h, 0\big)\,, \end{aligned} \tag{50}$$

where ϵ is given by (31). Approximate equations satisfied by the quantities v_1 to v_4 can be read off from Eq. (12); for example,

$$\lambda\, v_2 \simeq e^{-\beta F(\sigma_\epsilon - \frac{1}{2}\sigma)}\,(q_1 v_1 + q_2 v_3)\,. \tag{51}$$

In Eq. (51), the factors q_1 and q_2 arise from the integrations over y_0 and s_1 in Eq. (12), so they will be of order $(\beta F)^{-2}$ for sufficiently large F. The exponential factor, which corresponds to $\exp(-\beta F[s_2 + \sigma_{2,1}])$ in (12), can be transferred to the left-hand side of (51). By proceeding in this way for the remaining quantities v_i, we obtain a matrix eigenvalue equation

$$\lambda \mathsf{B}\mathbf{v} = \mathsf{K}\mathbf{v}\,, \tag{52}$$

where $\mathbf{v}$ is a vector with components v_i and the matrices K and B are given by

$$\mathsf{K} = \begin{pmatrix} 0 & q_1 & 0 & 0 \\ q_1 & 0 & q_2 & 0 \\ 0 & q_2 & q_3 & 0 \\ 0 & 0 & 0 & q_4 \end{pmatrix} \tag{53}$$

and

$$\mathsf{B} = \frac{1}{\sqrt{k}} \begin{pmatrix} k_\epsilon/k & 0 & 0 & 0 \\ 0 & k/k_\epsilon & 0 & 0 \\ 0 & 0 & 0 & 1 \\ 0 & 0 & 1 & 0 \end{pmatrix}, \tag{54}$$

where $k = \exp(-\beta F \sigma)$ and $k_\epsilon = \exp(-\beta F \sigma_\epsilon)$.

The symmetry of the matrix K is not obvious from the intuitive derivation given here. To refine the argument, it can be supposed that the eigenfunction u is approximated by a linear combination $u = \sum_i v_i b_i$ of localized functions $b_i(y_2, y_1, s_2)$. Projection of Eq. (12) onto the basis functions then leads to an equation of the form (52), in which the symmetry of the matrices B and K follows from the symmetry of the functionals $B[b_i, b_j]$ and $K[b_i, b_j]$ defined in Eqs. (18) and (22). It might therefore be an interesting task to construct a localized basis adapted to the special case $\phi \to \phi_{\max}$, but we do not attempt this here. Instead we proceed to the qualitative results that can be derived from the matrix eigenvalue equation (52).

The equation for λ, obtained from $\det(\mathsf{K} - \lambda\mathsf{B}) = 0$, is

$$\lambda^4 - (q_1^2 + q_3 q_4) k \lambda^2 - q_2^2 q_4 \sqrt{k}\, k_\epsilon \lambda + q_1^2 q_3 q_4 k^2 = 0\,. \tag{55}$$

To determine the form of the solutions of this equation, it is helpful first to introduce a scaled, dimensionless variable $\mu = \lambda/(q_2^2\, q_4\, \sqrt{k}\, k_\epsilon)^{1/3}$. Written in terms of μ, (55) becomes

$$\mu^4 - p_1 r \mu^2 - \mu + p_2 r^2 = 0\,, \tag{56}$$

where $r = (k/k_\epsilon)^{2/3} = \exp(-\beta F \Delta_d)$ is small and p_1 and p_2 are expected to be independent of F for large F.

In the limit $r \to 0$ (or $\beta F \Delta_d \to \infty$), the solutions of (56) are $\mu = 0$, 1, ω, and ω^2, where ω is a complex cube root of unity. For small r, the solutions can be expanded to first order in r, giving

$$\mu = 1 + \tfrac{1}{3} p_1 r,\ \omega + \tfrac{1}{3} p_1 \omega^2\, r,\ \omega^2 + \tfrac{1}{3} p_1 \omega\, r \tag{57}$$

for the three roots with modulus close to unity; the fourth root is of order r^2.

So far we have considered only the even-parity solutions of (12). The same method can be applied to the odd-parity solutions, which leads to a further three roots μ with modulus close to unity. These roots are given by the same expressions as in (57), but with the opposite signs. This leads to a two-fold degeneracy in $|\mu|$ for the real solutions and a four-fold degeneracy for the complex solutions. In our approximate treatment, the cause of the degeneracy is our selective use of configurations in which neighboring disks lie at (or near) opposite sides of the channel, so that perfect zigzag order is assumed. This assumption about the configurations is reasonable, given our knowledge that $\xi_{zz} \gg \xi_c$ for large F, but it does prevent us from estimating the correlation length ξ_{zz} from the ratio of the first two real eigenvalues.

The result that emerges from our analysis is that, for sufficiently large F, the six eigenvalues of largest magnitude are approximately $(-\omega)^n\, \lambda_1$, with $n = 0$ to 5. An observable such as y will have nonzero matrix elements between u_1 and the complex conjugate pair of eigenfunctions with $\mu \simeq -\omega$ and $-\omega^2$, which are the primitive sixth roots of unity. The correlation function $\langle y_i\, y_{i+s} \rangle$ will therefore contain a contribution that oscillates with period six in s.

To calculate the correlation length ξ_c we must go beyond the zeroth order in r and use the expressions given in Eq. (57). We find

$$\begin{aligned} \xi_c &\simeq 1/\ln([1 + \tfrac{1}{3} p_1 r]/|\omega + \tfrac{1}{3} p_1 \omega^2\, r|) \\ &\simeq \frac{2}{p_1} \exp(\beta F \Delta_d)\,, \end{aligned} \tag{58}$$

which is of the form anticipated in (47), though we have not determined the quantity p_1, which will be a function only of the ratio h/σ.

Finally, we use the large-F approximation

$$\lambda_1 \simeq \left(q_2^2\, q_4\, \sqrt{k}\, k_\epsilon\right)^{1/3} \tag{59}$$

to derive the equation of state for $\phi \to \phi_{\max}$. The free energy per disk is given by

$$\begin{aligned} \beta\Phi/N &= -\ln \lambda_1 \\ &= -\tfrac{1}{3} \ln\left(q_2^2\, q_4\, \sqrt{k}\, k_\epsilon\right) \\ &= \tfrac{1}{6} \beta F (\sigma + 2\sigma_\epsilon) + 2 \ln(\beta F) + \mathrm{O}(1)\,, \end{aligned} \tag{60}$$

in which the F-dependence of q_2 and q_4 has been used to obtain the coefficient of the logarithmic term; the contribution written as O(1) contains only terms that do not increase with F. Differentiation of Φ with respect to F (cf. Eq. (15)) gives the equation of state

$$\beta F \simeq \frac{2N}{L - \frac{1}{6} N a} = \frac{d_{\rm eff} N}{L(1 - \phi/\phi_{\max})} \tag{61}$$

expected on the general grounds discussed in Ref. [40]. The factor $d_{\rm eff} = 2$ in the expression for the force is the same coefficient 2 that multiplies $\ln(\beta F)$ in Eq. (60). In the context of our derivation, the source of this factor is the two-fold integration in Eq. (12), where the eigenfunction is localized within regions whose widths are proportional to $(\beta F)^{-1}$.

VIII. DISCUSSION

We have solved the transfer integral equation appropriate to disks moving in a channel of a width which permits NNN contacts and we have determined its thermodynamic properties and some of its correlation lengths numerically exactly. The most striking feature of our results are those connected with the features at ϕ_d and at ϕ_K.

The packing fraction ϕ_d marks the point at which bond-orientational order (i.e. zigzag order) sets in, and will be where the dynamics of the system will start to become activated. We believe that if the channel width were increased this feature would evolve into the fluid–hexatic phase transition of hard disks [38]. The new feature, which is absent for narrower channels with only NN contacts, is that at ϕ_K. We believe it would evolve for wider channels into the hexatic–crystal phase transition [38]. It has a clear connection with the development of structural order.

Despite being of structural origin, the behavior near ϕ_K mimics that normally associated with the ideal glass transition. At the ideal glass transition, a divergence of the point-to-set length scale is expected [14, 15] and this will be accompanied by a divergence of the penetration length for amorphous order [16]. A review of some of the length scales which are perhaps of relevance to amorphous systems can be found in Ref. [44]. This penetration length is the distance over which the effect of a boundary condition (imposed by freezing the positions of a subset of spheres) extends into the liquid; for the case of three dimensions it has been determined from molecular dynamics simulations by Gradenigo et al. [12] and by Berthier and Kob [13]. For our system of disks in a channel, freezing the positions of the disks in the region $x < 0$ supplies a boundary condition for the motion of the mobile disks in the region $x > 0$: in particular, it fixes the nearest-neighbor separation near $x = 0$. Following the discussion in Secs. IV and VI, the time-averaged nearest-neighbor separations $\langle x_{k+1} - x_k \rangle$ will approach the bulk value L/N as $(-1)^k \exp(-k/\xi_3)$ for large k, so that we can identify the penetration length with ξ_3.

At the ideal glass transition it is expected that the relaxation time τ_α should diverge [6]. It is argued in Refs. [1, 2] that τ_α is the time at which a disk can escape its cage by crossing from one side of the channel to the other. Within transition-state theory, whose accuracy for a system of hard disks has been tested in Ref. [45], τ_α is given by

$$\tau_\alpha \sim \exp(\beta F \Delta_b), \tag{62}$$

where the length Δ_b is $\mathrm{O}(\sigma)$, as discussed in Ref. [1] for the case of nearest-neighbor interactions. On using Eq. (35) for F, the relaxation time will *appear* to diverge in a Vogel–Fulcher manner of Eq. (1) for a range of ϕ less than ϕ_K. Note that at ϕ_K it will be a very challenging problem to study the properties of the equilibrated system by molecular dynamics: the densities are so close to $\phi_{\max}$ that the time scales in the system will be extremely long. Any real divergence of τ_α will, of course, be avoided in the narrow channel systems, and we suspect that it might also be avoided for hard spheres in three dimensions [10, 11].

Above the ideal glass transition discussed in the infinite dimensional limit, i.e. when $\phi > \phi_K$, particles are expected to be caged near their initial positions forever, whereas for $\phi < \phi_K$, the particles can escape to infinity. In our narrow channel system, the particles are in one sense caged for all time as they cannot pass each other; nevertheless, we have seen in Sec. V that there is a qualitative difference in the nature of the confinement above and below ϕ_K. Below ϕ_K, the nearest-neighbor separations in the x-direction fluctuate as $1/\sqrt{F}$, whereas above ϕ_K the fluctuations are smaller and will decrease as $1/F$ as $\phi \to \phi_{\max}$. Similarly, there is a change in the nature of the fluctuations in the y-direction on passing through ϕ_K. Below ϕ_K the fluctuations in y are small but of order σ; above ϕ_K, they will shrink at large F like those of the x-component, as $1/F$.

Thus many properties of our system are similar to the properties of real glasses. One notable difference between our channel system and the three dimensional hard sphere system is that in the latter system, glass behavior occurs in the supercooled metastable region at densities above that of the fluid-crystal transition. Our own work is a study of equilibrium behavior, in which the long-lived metastable states are simply included in the thermal average. But there are parallels nonetheless between the two types of system above ϕ_K: as the packing fraction increases towards its maximum value, both systems develop a jammed crystal ordering.

One of our observations is that the structural feature which is behind the onset of activated dynamics at ϕ_d, which is bond-orientational order in the channel problem, is not the same as the structural feature which produces our ϕ_K. It is possible that something similar may occur in three dimensional glasses, but simulations of them at ϕ_K are difficult, so that the situation remains unclear, like much else in the study of glasses.

Acknowledgments

We should like to thank Richard Bowles for supplying information on the nature of the kink in the complexity $S_c(\phi)$.

[1] M. J. Godfrey and M. A. Moore, Phys. Rev. E **89**, 032111 (2014).
[2] J. Robinson, M. J. Godfrey, and M. A. Moore, arXiv:1501.03738
[3] R. K. Bowles and I. Saika-Voivod, Phys. Rev. E **73**, 011503 (2006).
[4] M. Z. Yamchi, S. S. Ashwin and R. K. Bowles, Phys. Rev. Lett. **109**, 225701 (2012).
[5] S. S. Ashwin, M. Zaeifi Yamchi, and R. K. Bowles, Phys. Rev. Lett. **110**, 145701 (2013).

[6] G. Parisi and F. Zamponi, Rev. Mod. Phys. **82**, 789 (2010).
[7] J. A. Cuesta and A. Sánchez, J. Stat. Phys. **115**, 869 (2004).
[8] L. Berthier, Phys. Rev. Lett. **112**, 220602 (2014)
[9] L. Santen and W. Krauth, arXiv:cond-mat/0107459
[10] M. A. Moore, Phys. Rev. Lett. **96**, 137202 (2006).
[11] J. Yeo and M. A. Moore, Phys. Rev. B **85**, 100405(R) (2012).
[12] G. Gradenigo, R. Trozzo, A. Cavagna, T. S. Grigera, and P. Verrocchio, J. Chem. Phys. **138**, 12A509 (2013).
[13] L. Berthier and W. Kob, Phys. Rev. E **85**, 011102 (2012). Note that these authors denote the penetration length by $\xi_{\rm stat}$, calling it "the point-to-set static length scale".
[14] C. Cammarota, A. Cavagna, G. Gradenigo, T. S. Grigera, and P. Verrocchio, J. Chem. Phys.. **131**, 194901 (2009); J. Stat. Mech. L12002 (2009).
[15] A. Cavagna, T. S. Grigera, and P. Verrochio, J. Chem. Phys. **136**, 204502 (2012).
[16] C. Cammarota, G. Biroli, M. Tarzia, and G. Tarjus, Phys. Rev. Lett. **106**, 115705 (2011).
[17] G. Tarjus, S. A. Kivelson, Z. Nussinov, and P. Viot, J. Phys.: Condens. Matter **17**, R1143 (2005).
[18] C. P. Royall and S. R. Williams, Phys. Rep. **560**, 1 (2015).
[19] C. P. Royall, A. Malins, A. J. Dunleavy, and R. Pinney, J. Non-Cryst. Solids **407**, 34 (2015).
[20] E. D. Cubuk, S. S. Schoenholz, J. M. Rieser, B. D. Malone, J. Rottler, D. J. Durian, E. Kaxiras, and A. J. Liu, arXiv:1409.6820.
[21] S. S. Ashwin and R. K. Bowles, Phys. Rev. Lett. **102**, 235701 (2009).
[22] J. D. Bernal, Nature **185**, 68 (1960).
[23] Y. Jin and H. A. Makse, Physica A **389**, 5362 (2010).
[24] B. D. Lubachevsky and F. H. Stillinger, J. Stat. Phys. **60**, 561 (1990).
[25] D. Frenkel, http://www.condmatjournalclub.org/?p=93.
[26] R. D. Kamien and A. J. Liu, Phys. Rev. Lett. **99**, 155501 (2007).
[27] E. Eisenberg and A. Baram, Proc. Natl. Acad. Sci. U.S.A. **104**, 5755 (2007).
[28] Ch. Forster, D. Mukamel, and H. A. Posch, Phys. Rev. E **69**, 066124 (2004).
[29] J. A. Barker, Aust. J. Phys. **15**, 127 (1962).
[30] D. A. Kofke and A. J. Post, J. Chem. Phys. **98**, 4853 (1993).
[31] S. Varga, G. Balló, and P. Gurin, J. Stat. Mech. **2011**, 11006 (2011).
[32] Φ differs from the Gibbs free energy by an additive term that depends only on N and β. This is because the canonical partition function differs from the configuration integral by $2N$ factors of the thermal wavelength, $(2\pi\beta\hbar^2/m)^{1/2}$.
[33] J. L. Lebowitz, Phys. Fluids **3**, 64 (1960).
[34] J. K. Percus, J. Stat. Phys. **15**, 423 (1976).
[35] R. B. Lehoucq, D. C. Sorensen, and C. Yang, *ARPACK Users' Guide* (SIAM, Philadelphia, 1998)
[36] W. E. Arnoldi, Quarterly of Applied Mathematics **9**, 17 (1951); Y. Saad, *Numerical Methods for Large Eigenvalue Problems* (SIAM, Philadelphia, 2011).
[37] J. Kolafa and M. Rottner, Molecular Physics **104**, 3435 (2006).
[38] E. P. Bernard and W. Krauth, Phys. Rev. Lett. **107**, 155704 (2011).
[39] H. Au-Yang and M. E. Fisher, Phys, Rev. B **11**, 3469 (1975).
[40] Z. W. Salsburg and W. W. Wood, J. Chem. Phys. **37**, 798 (1962).
[41] M. Maiti and S. Sastry, J. Chem. Phys. **141**, 044510 (2014).
[42] P. Gurin and S. Varga, J. Chem. Phys. **139**, 244708 (2013).
[43] The expression for Δ_a is different in the nearest-neighbor case discussed in Ref. [1]. For $h < \sqrt{3}\sigma/2$, removing a disk from one side of the channel leaves a gap of length $2\sqrt{\sigma^2 - h^2} - \sigma$. After this gap has been closed, the net increase in length per defect is $\Delta_a = \sigma - \sqrt{\sigma^2 - h^2}$.
[44] J. Kurchan and D. Levine, J. Phys. A: Math. Theor. **44**, 035001 (2011).
[45] M. Barnett-Jones, P. A. Dickinson, M. J. Godfrey, T. Grundy, and M. A. Moore, Phys. Rev. E **88**, 052132 (2013).